Thermal-Dependent Two-Dimensional (2-D) Magneto-Micropolar Fluid Flow over Stretching Surfaces in Porous Media: Optimal Homotopy Analysis Method (OHAM)-Based Analysis with Viscous Dissipation and Radiation Effects

Hussain Basha[1, *], V. Ramanjini[2]

[1] Department of Mathematics, Government First Grade College, Zalaki-586204, Vijayapur, Karnataka, India

[2] Department of Mathematics, Government First Grade College, Lingasuguru, Raichur –584 122, Karnataka, India

[*]Corresponding author: hussain555basha@gmail.com

Abstract

The current investigation explores the thermal convection characteristics of a magneto-micropolar fluid with temperature-sensitive properties flowing over an elastically deformable porous-embedded surface. The mathematical model incorporates frictional heating effects, internal thermal energy variation (generation/absorption), and optically thick radiative flux described by the Rosseland approximation. The resultant coupled nonlinear system is tackled analytically through the Optimal Homotopy Analysis Method (OHAM), which provides convergent series-based solutions. The resulting velocity, microrotation, and temperature fields are illustrated through graphical and tabulated data across a broad range of physical parameters. Validation against existing literature demonstrates the reliability of the present approach. Quantitative analysis shows that the microrotation boundary layer decreases by approximately 18–25% with increasing micropolar parameter, while thermal boundary layer thickness increases by about 10–14% under stronger radiative effects. Moreover, micropolar fluids exhibit a thinner momentum boundary layer compared to Newtonian fluids under identical conditions. Specifically, the Newtonian case $K = 0$ yields a thinner layer relative to the micropolar case $K > 0$. Overall, the results provide valuable insights into micropolar fluid behavior with practical implications in porous and radiative flow systems.

Keywords: magneto-micropolar fluid, viscous dissipation, thermal radiation, heat generation or absorption, OHAM

1. Introduction

The Pioneering researchers and process engineers are focused on improving drying and cooling operations in industrial manufacturing, where the cooling rate and deformation behavior are critical factors that determine the final product quality. The thermal and hydrodynamic behavior of fluids flowing over a continuously deforming stretching sheet has been a subject of sustained scientific interest, primarily owing to its widespread relevance in polymer extrusion, metal rolling, and textile manufacturing. As a consequence, the foundational contribution of Sakiadis [1] established the boundary layer framework for a moving continuous surface, providing the first systematic analysis of such flows at constant surface velocity. Extending the Sakiadis framework, Crane [2] derived a closed-form exact solution for viscous fluid motion over a linearly stretching plate, a result that served as the cornerstone for subsequent analytical investigations. Gupta and Gupta [3] examined the combined heat and mass transport over a stretching surface incorporating wall suction and blowing, demonstrating that transpiration conditions substantially modify boundary layer thickness and convective transport. Their groundbreaking work pioneered the first ever analytical basis for analysis of stretching sheet problems. Grubka and Bobba [4] analytically characterized the thermal response of a continuous stretching surface under power-law surface temperature variations, establishing benchmark solutions for subsequent researchers. Their work showed that the heat transfer and temperature distribution are significantly affected by the variation of surface temperature, which became a reference point for subsequent stretching-sheet researches. Dutta et al. [5] constructed an exact analytical solution for the temperature distribution induced by a uniform heat flux condition over a stretching surface, offering precise insights into heat transfer under constant flux scenarios. Chen and Char [6] investigated thermal transport phenomena on a continuously stretched surface subject to wall suction and injection, deriving analytical expressions that quantified the contrasting influence of these transpiration conditions on thermal boundary layer development. Ali [7] presented numerical solutions for a range of thermal boundary conditions while examining the heat transmission properties of a continually extending surface. The rheological frameworks such as Oldroyd-B, Maxwell, and Jeffery models, along with Cattaneo–Christov modified Fourier heat flux theory, have been widely adopted to capture the diverse non-Newtonian characteristics observed in industrial flow systems [8–13].

Nonetheless, other types of non-Newtonian fluids are widely used for engineering and industrial applications due to their practicality and convenience. For non-Newtonian fluids, the shear strain rate-to-shear rate ratio is not constant at a specific temperature, but it also varies with the manner of flow. To study such behavior, different non-Newtonian fluid models are proposed in the literature, such as the

viscoelastic liquid model, the second-order liquid model, Walter's liquid model, the Maxwell liquid model, the Cattaneo-Christove heat flux model, etc. Furthermore, the advantages of Navier's theory are not valid for the fluids with micro-rotation, microstructure, rotational inertia, couple stress, and body torque, which are connected with the micropolar liquid model. Micropolar fluids; in order to investigate the behavior of micro-rotation and micro-inertia in such fluids as fluid suspensions, colloidal solutions, liquid crystals, blood of animals, paint, etc., Eringen [14–15] proposed micropolar fluids. Gorla et al. [16] presented the solutions for boundary layer steady state temperature transfer with a coating surface and viscous dissipation effects on a micro-polar liquid over a semi-infinite flat plate.Many scientists have worked on micropolar fluids with different geometries, such as [17-22].

On the other hand, the current results are directly applicable to industrial processes in which the temperature-dependent transport properties and magnetic actuation play a critical role. For instance, in hot rolling and polymer extrusion, control of surface temperature and flow behavior is essential to obtaining the appropriate product thickness, surface finish, and material strength. One may also note other applications where knowledge about varying viscosity/thermal conductivity, such as cooling in MHD metal casting or nanofluid coating, makes an impact on the heat transfer and is labelled as an important tool to produce high quality material and a stable process. The implication of the work outlined above is that the current results are rich in terms of providing ideas for efficiency (heat transfer) enhancement in actual practical manufacturing and thermal processing applications. The Flows have been studied by several workers and thus reported due to the fact that most of the applications are subject to appreciable variation in temperature (see e.g. [23-26]).

The relevance of the present work lies in the study of the changeable thermo-physical properties of magneto-convection micropolar fluid flow past an extending sheet with a porous medium in the presence of viscous dissipation, internal heat, and thermal radiation effects. Further, the porous media emphasize the relevance of the present model in potential industrial and engineering applications of micropolar fluid flow such as geothermal energy extraction, filtration processes, polymer processing, petroleum reservoir engineering, cooling of electronic devices, and biomedical transport phenomena**,** where porous structures and micro-structural fluid behavior play an important role. These additions help to better connect the theoretical findings with practical applications. Furthermore, the governing coupled nonlinear ordinary differential equation system is solved using OHAM, following the computational strategies established in [27–32]. Graphs and tables are provided to give a sense of how embedding parameters affect results.

2. Mathematical Formulation

The present two-dimensional model for incompressible micropolar fluid motion over a permeable elastic stretching surface accounts for Ohmic dissipation, internal heat source or sink, and radiative thermal transport through an optically opaque porous matrix. A physical realization of this work is presented in Figure 1, where the flow field is demonstrated to be perpendicular to the y-axis and parallel to the x direction and possessing the prescribed x and y components of velocity.

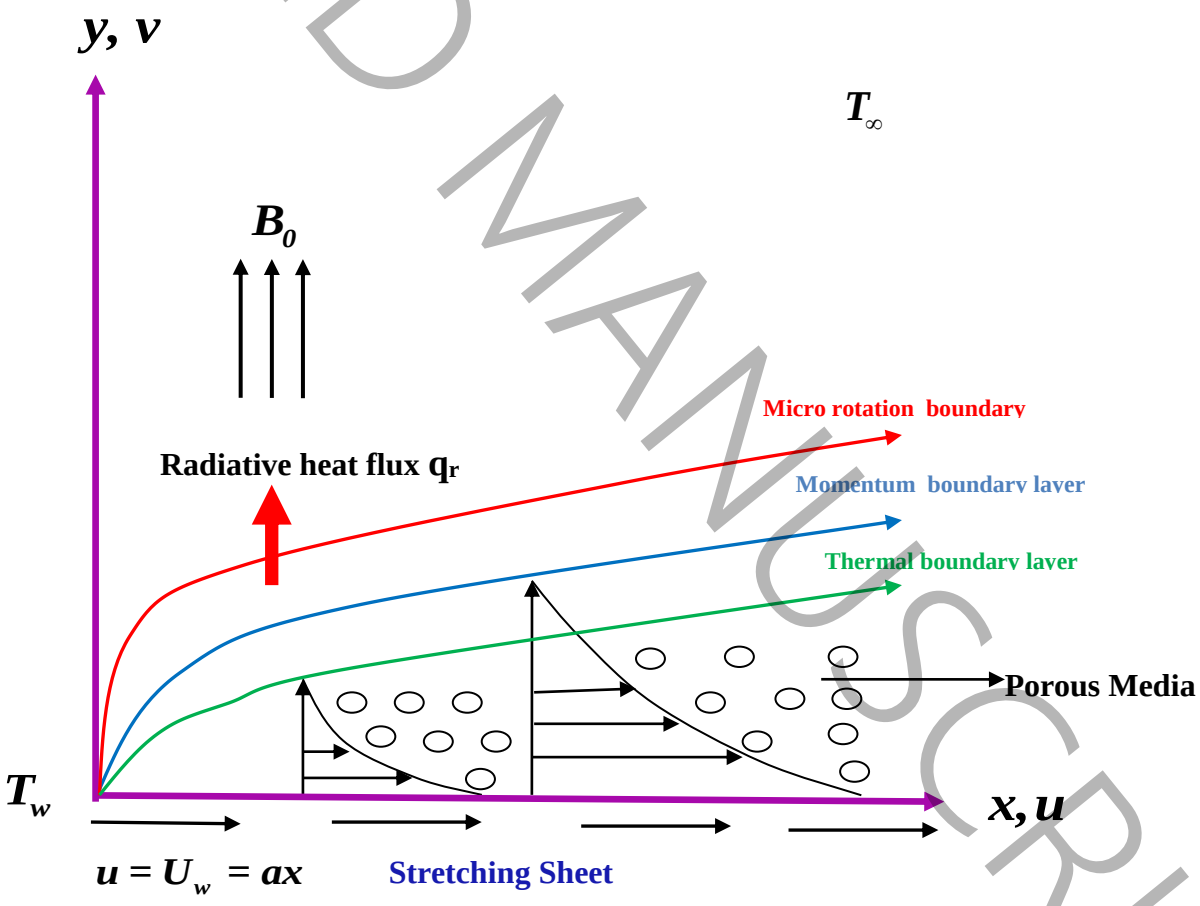

Fig. 1: Schematically illustrates the physical configuration

A transverse uniform magnetic field is oriented perpendicular to the stretching surface along the y-direction; the induced magnetic field is neglected under the assumption of small magnetic Reynolds number. We take the external flow velocity as zero but the stretchable velocity as $U_w = ax$. The PST $T = T_w = T_\infty + A\left(x/l\right)^2$ (Prescribed power law surface temperature) is proposed here to investigate the temperature field, transfer of temperature. In addition the micro-particles $N = N\left(x, y\right)$ angular velocity is utilized. The temperature-sensitive parameters of the transport fluids, thermal conductivity $K\left(T\right)$ and viscosity $\mu\left(T\right)$, are considered in this study. The linear temperature-dependent models for viscosity and thermal conductivity are adopted (see Eqs. (5)–(6)), which are widely accepted for moderate temperature variations due to their mathematical simplicity and proven accuracy in boundary-layer flows. Although nonlinear relations (e.g., quadratic or exponential forms) may offer improved precision for large temperature gradients, they substantially increase model complexity and often require purely numerical approaches. Therefore, the linear formulation provides a practical balance between physical realism and analytical tractability for the current problem.

Under the standard boundary-layer approximations and Boussinesq assumptions, the governing conservation equations for mass, momentum, angular momentum, and energy take the following form:

$$\frac{\partial u}{\partial x} + \frac{\partial \mathrm{v}}{\partial y} = 0 \tag{1}$$

$$u\frac{\partial u}{\partial x} + \mathrm{v}\frac{\partial u}{\partial y} = \frac{1}{\rho}\frac{\partial}{\partial y}\left(\mu\left(T\right)\frac{\partial u}{\partial y}\right) + \frac{k}{\rho}\left(\frac{\partial^2 u}{\partial y^2} + \frac{\partial N}{\partial y}\right) - \left(\frac{\mu\left(T\right)+k}{\rho K_p}\right)u - \frac{\sigma B_0^2}{\rho}u \tag{2}$$

$$u\frac{\partial N}{\partial x} + \mathrm{v}\frac{\partial N}{\partial y} = \frac{1}{\rho j}\left(\frac{\partial}{\partial y}\left(\gamma\frac{\partial N}{\partial y}\right)\right) - \frac{k}{\rho j}\left(2N + \frac{\partial u}{\partial y}\right) \tag{3}$$

$$u\frac{\partial T}{\partial x} + \mathrm{v}\frac{\partial T}{\partial y} = \left(\rho C_p\right)^{-1}\frac{\partial}{\partial y}\left(K\left(T\right)\frac{\partial T}{\partial y}\right) - \frac{1}{\partial C_p}\frac{\partial q_r}{\partial y} + \left(\rho C_p\right)^{-1}\left(\mu\left(T\right)+K\left(T\right)\right)\left(\frac{\partial u}{\partial y}\right)^2 + \frac{Q}{\rho c_p}\left(T - T_\infty\right) \tag{4}$$

Affording to numerous publications [23, 24] the expression for the heat-dependent viscosity $\mu\left(T\right)$ is

$$\mu\left(T\right) = \frac{\mu_o}{1+\beta\left(T - T_\infty\right)} \tag{5}$$

As well, the linear expression for the relationship between heat conductivity and temperature is

$$\left(T_w - T_\infty\right)/K_\infty = \left[\left(T_w - T_\infty\right) + \varepsilon\left(T - T_\infty\right)\right]/K\left(T\right) \tag{6}$$

Similarly, following is a description of the Rosseland approximation is a classical diffusion-type approximation used to simplify radiative heat flux in a participating medium.The limitations of Rosseland approximations. It is important to note that the Rosseland diffusion approximation is strictly valid foroptically thick media and relatively small temperature gradients**,** where radiative heat transfer behaves similarly to a diffusion process. Under conditions of very strong temperature gradients or optically thin media**,** the approximation may lose accuracy because the radiative heat flux can no longer be represented adequately by the linearized temperature formulation. Moreover, it replaces the radiative heat flux q_r with a conduction-like diffusion term:

$$q_r = -\frac{16\sigma T^3}{3\alpha}\nabla T \tag{7}$$

here, σ denotes the Stefan–Boltzmann constant, α is represents the Rosseland mean spectral absorption coefficient, and T is the local absolute temperature of the fluid.

For linearization process, we need to take divergence of radiative flux:

$$\nabla.q_r = -\nabla.\left(\frac{16\sigma T^3}{3\alpha}\nabla T\right)$$

For negligible small heat variations around a reference temperature T_∞, we can linearize $T^4 \approx 4T_\infty{}^3 - 3T_\infty{}^4$

, which gives $\nabla.q_r \approx -\left(\frac{16\sigma T_\infty{}^3}{3\alpha}\nabla^2 T\right)$

The problem under consideration's physical Boundary Conditions (BC's) are given by

$$\begin{aligned} &u = U_w = ax,\ \mathrm{v} = 0,\quad N/-n = \frac{\partial u}{\partial y} \quad \text{at} \quad y = 0 \\ &u,\ N \to 0, \quad as \quad y \to \infty \end{aligned} \tag{8}$$

The thermal boundary conditions associated with Eq. (4) are formulated in accordance with the prescribed surface temperature (PST) heating mechanism adopted in the present study.

$$\left.\begin{aligned} &T = T_w = T_\infty + A_1\left(x/l\right)^2, \quad \text{at} \quad y = 0 \\ &T \to T_\infty, \quad \text{as} \quad \mathrm{y} \to \infty \end{aligned}\right\} \tag{9}$$

Here, from Eqs. (1-9), a is constant and $a > 0$, U_w is the velocity (free-stream), ρ is the fluid density,

u and v are the velocity components in x and y directions respectively, in the above equations, k is the vertex viscosity, N is the microrotation angular velocity component, T is the local fluid temperature, B_0 is the applied magnetic field intensity, C_p represents the isobaric specific heat capacity of the fluid, T_w denotes the surface wall temperature, T_∞ is the ambient free-stream temperature far from the stretching surface, Q is the heat generation or absorption coefficient, K_p denotes the permeability of the porous layer, j is the microinertial density per unit mass and the spin-gradient viscosity γ is related to the dynamic viscocity and microinertia through the constitute relation $\gamma = \left(\mu(t) + k/2\right) j$ .Similarly, in equation (8),the parameter n represents the micropolar boundary parameter and varies within the range $0 \le n \le 1$. The boundary condition n = 0 physically implies that microelements near the solid wall are unable to rotate, reflecting a condition of concentrated particle suspension at the surface with vanishing micro-rotation. The case n = 0.5 is often associated with turbulence-like behavior in the boundary layer, where micro-rotation effects are more pronounced. When n=1, it characterizes a weak concentration of microelements at the wall, corresponding to a stress-free or free-spin condition and it controls the micro-rotation boundary behavior in the governing equations. μ_0 is the ambient fluid viscosity, K_∞ is thermal conductivity for away from the plate, ε is variable thermal conductivity parameter, l denotes the characteristic length, q_w is the heat flux, while A and D are constants.

The set of equations (1)-(4) are converted into a dimensionless form. To do this the following similarity transformations are considered (see details in Fatunmbi and Okayo [24])

$$u = \frac{\partial \psi}{\partial y} = axf'(\eta),\ \mathrm{v} = -\frac{\partial \psi}{\partial x} = -\sqrt{av}\, f(\eta),\ \eta = \sqrt{\frac{a}{\nu}}y,\ N = ax\, g(\eta)\sqrt{\frac{a}{\nu}},$$
$$\theta(\eta) = \frac{T - T_\infty}{T_w - T_\infty},\quad T_w - T_\infty = \sqrt{\frac{\nu}{a}}\frac{q_w}{K_\infty}, \tag{10}$$

where $f \,\&\, \theta$ denote the dimensionless stream function and temperature, respectively. The continuity equation is identically satisfied by the introduction of the stream function. Substituting the transformations of Eq. (10) together with the constitutive relations (5)–(7) into the governing partial differential equations (2)–(4) yields the following system of nonlinear ordinary differential equations.

$$\left(1+h\theta\right)\left[\left(1+\left(1+h\theta\right)K\right)f''' + \left(1+h\theta\right)\left(ff'' - f'^2 + Kg\right) - \left(Da + \left(K+M\right)\left(1+h\theta\right)\right)f'\right] - h\theta' f'' = 0 \tag{11}$$

$$(1+h\theta)\left[\left(1+(1+h\theta)+\frac{K}{2}\right)g''+(1+h\theta)\left(fg'-f'g-K\left(2g+f''\right)\right)\right]-h\theta' g'=0 \tag{12}$$

$$(1+h\theta)\left[(1+\varepsilon\theta+Nr)\theta''+\varepsilon\theta'^{2}+\Pr\left(f\theta'-2\theta f'+Q\theta\right)\right]+\Pr Ec\left(1+K\left(1+h\theta\right)\right)f''^{2}=0 \tag{13}$$

And respective BC's are transformed to,

$$\begin{aligned} &f'(0)=1,\ f(0)=g(0)+nf''(0)=0, \text{and} \quad \theta(0)=1 \\ &f'(\infty), g(\infty), \theta(\infty)\to 0 \end{aligned} \tag{14}$$

The BC's used in the present study represent practical engineering situations such as stretching surfaces encountered in polymer extrusion, coating processes, and cooling of continuous sheets, where the fluid adheres to the surface and experiences strong shear. Additionally, the far-field conditions correspond to the ambient quiescent fluid region where the effects of surface motion gradually vanish, which is consistent with boundary-layer flow assumptions commonly used in engineering analyses.

Additionally, where h is the temperature dependent viscosity parameter, K is micro-polar parameter, Da is Darcy parameter, Pr denotes the Prandtl number, M denotes the magnetic parameter, Nr defines the radiation parameter, Q is heat source/sink parameter and Ec is Eckert number, which are given by

$$\begin{aligned} &h=\beta\left(T_w-T_\infty\right), K=\frac{k}{\mu_0}, Da=\frac{v}{aK_p}, \Pr=\frac{\mu_0 C_p}{K_\infty}, M=\frac{\sigma B_0{}^2}{a\rho}, \\ &Nr=\frac{16\sigma T_\infty{}^3}{3\alpha K_\infty}, Q=\frac{Q}{a\rho C_p},\ Ec=\frac{U_w{}^2}{C_p\left(T_w-T_\infty\right)} \end{aligned} \tag{15}$$

The primary engineering quantities of practical interest in the present problem are the local skin friction coefficient C_f, the surface couple stress M_w, and the local Nusselt number Nu_x, which respectively characterize the wall shear force, microrotational stress, and convective heat exchange at the surface.

$$C_f=\frac{\tau_w}{\rho U_w{}^2}, Nu_x=\frac{xq_w}{K_\infty\left(T_w-T_\infty\right)}, C_s=\frac{xM_w}{\mu ja} \tag{16}$$

Where, wall shear stress τ_w is given by $\tau_w=\left[\left(\mu+k\right)\partial u/\partial y+kN\right]_{y=0}$, heat flux at the surface q_w is given by $q_w=-K_\infty\left[\left(1+Nr\right)\partial T/\partial y\right]_{y=0}$ and wall couple stress M_w is given by $M_w=\left[\gamma\,\partial N/\partial y\right]_{y=0}$.

After using the scaling variables, the skin friction coefficient, wall couple stress and Nusselt number is transformed to

$$C_f{}^*=f''(0),\ C_s{}^*=g'(0), Nu_x{}^*=-\theta'(0), \tag{17}$$

Where

$$C_f = \frac{(1+h)C_f\sqrt{\mathrm{Re}_x}}{1+K/2}, \quad Nu_x = \frac{Nu_x}{(1+Nr)\sqrt{\mathrm{Re}_x}}, \; C_s = \frac{(1+h)C_s}{(1+K/2)\sqrt{\mathrm{Re}_x}} \tag{18}$$

3. Method of solution

The strongly nonlinear boundary value problem (BVP) defined by Eqs. (11)–(13) subject to conditions (14) is resolved using the Optimal Homotopy Analysis Method (OHAM), a powerful semi-analytical technique that offers guaranteed convergence for highly nonlinear systems with the help of software named MATHEMATICA 10. This method exploits a continuous deformation mapping from a tractable linear problem to the target nonlinear system, yielding uniformly convergent series solutions even when perturbation-based methods fail. A distinguishing advantage of OHAM lies in the flexibility it affords in selecting auxiliary linear operators and initial approximations. The convergence-control parameters (CCPs), embedded in the homotopy. The OHAM has been successfully applied to different types of nonlinear coupled problems (for more details refer to [27-32]). In view of these results, we noted that the OHAM overcomes the restrictions of all other analytical approximation methods for highly nonlinear problems. Guided by the boundary conditions (14) and the expected physical behavior of the solution, the following initial approximations and auxiliary linear operators are chosen for f, g and θ.

$$f_0(\eta) = (1-e^{-\eta}), \;\; g_0(\eta) = \omega e^{-\eta} + \left(\frac{\eta}{2}\right)e^{-\eta}, \;\; h_0(\eta) = e^{-\eta} \text{ and } \theta_0(\eta) = e^{-\eta} \tag{19}$$

The corresponding linear differential operators, consistent with the selected initial guesses, are defined as

$$\mathcal{L}_f = f''' - f', \; \mathcal{L}_g = (g'' - g) - e^{-\eta}, \mathcal{L}_h = h'' - h \text{ and } \mathcal{L}_\theta = \theta'' - \theta. \tag{20}$$

Zeroth-order deformation equations governing the homotopy family for the present system are formulated as,

$$\begin{aligned}
&(1-q)L_f\left[f(\eta;q) - f_0(\eta)\right] = qH_f(\eta)\hbar_f N_f\left[f(\eta;q), g(\eta;q), h(\eta;q)\theta(\eta;q),\right],\\
&(1-q)L_g\left[g(\eta;q) - g_0(\eta)\right] = qH_g(\eta)\hbar_g N_g\left[g(\eta;q), h(\eta;q), \theta(\eta;q), f(\eta;q)\right],\\
&(1-q)L_h\left[h(\eta;q) - h_0(\eta)\right] = qH_h(\eta)\hbar_h N_h\left[g(\eta;q), h(\eta;q), \theta(\eta;q), f(\eta;q)\right],\\
&(1-q)L_\theta\left[\theta(\eta;q) - \theta_0(\eta)\right] = qH_\theta(\eta)\hbar_\theta N_\theta\left[\theta(\eta;q), h(\eta;q), f(\eta;q), g(\eta;q)\right].
\end{aligned} \tag{21}$$

Now $H_f(\eta) = H_g(\eta) = H_h(\eta) = H_\theta(\eta) = e^{-\eta}$ are chosen as the auxiliary functions.

The parameter q [0, 1] serves as the homotopy embedding parameter; when $q = 0$, the system reduces to the linearized problem, while $q = 1$ recovers the original nonlinear formulation and $(\hbar_f, \hbar_g, \hbar_h, \hbar_\theta) \neq 0$ are called convergence control parameters (CCPs). Then these governing equations can be expand by Taylor series solution in-terms of embedding parameter *q*,

$$
\begin{aligned}
f(\eta;q) &= f_0(\eta) + \sum_{n=1}^{\infty} f_n(\eta) q^n, \\
g(\eta;q) &= g_0(\eta) + \sum_{n=1}^{\infty} g_n(\eta) q^n \\
h(\eta;q) &= h_0(\eta) + \sum_{n=1}^{\infty} h_n(\eta) q^n \text{ and} \\
\theta(\eta;q) &= \theta_0(\eta) + \sum_{n=1}^{\infty} \theta_n(\eta) q^n
\end{aligned} \tag{22}
$$

Practically, these can be calculating finitely many terms in the form of series solution. Therefore k^{th} approximate solution form a partial sums which can be given as,

$$
\begin{aligned}
f_{[k]}(\eta) &= f_0(\eta) + \sum_{n=1}^{k} f_n(\eta) \,, \\
g_{[k]}(\eta) &= g_0(\eta) + \sum_{n=1}^{k} g_n(\eta) \\
h_{[k]}(\eta) &= h_0(\eta) + \sum_{n=1}^{k} h_n(\eta) \;\& \\
\theta_{[k]}(\eta) &= \theta_0(\eta) + \sum_{n=1}^{k} \theta_n(\eta).
\end{aligned} \tag{23}
$$

where,

$$
f_n(\eta) = \frac{1}{n!} \frac{d^n f(\eta,q)}{d\eta^n}\bigg|_{q=0} \,,\; g_n(\eta) = \frac{1}{n!} \frac{d^n g(\eta,q)}{d\eta^n}\bigg|_{q=0},
$$

$$
h_n(\eta) = \frac{1}{n!} \frac{d^n \theta(\eta,q)}{d\eta^n}\bigg|_{q=0} \,, \theta_n(\eta) = \frac{1}{n!} \frac{d^n \phi(\eta,q)}{d\eta^n}\bigg|_{q=0}
$$

The optimal values of the CCPs are determined by minimizing the total average squared residual error, computed at each approximation order. This optimization process ensures that the solution series attains its fastest and most accurate convergence.

$$
\begin{aligned}
&L_f\left[f_p(\eta) - \chi_p \, f_{p-1}(\eta) \right] = \hbar_f R_m^f(\eta) \\
&L_g\left[g_p(\eta) - \chi_p \, g_{p-1}(\eta) \right] = \hbar_g R_m^g(\eta) \\
&L_h\left[h_p(\eta) - \chi_p \, h_{p-1}(\eta) \right] = \hbar_h R_m^h(\eta) \\
&L_\theta\left[\theta_p(\eta) - \chi_p \, \theta_{p-1}(\eta) \right] = \hbar_\theta R_m^\theta(\eta)
\end{aligned} \tag{24}
$$

$$
f_p'(0) = 1, \quad f_p(0) = g_p(0) + n f_p'', \;\; \theta_p(0) = 1,
$$
$$
f_p(\infty) = 0, \quad g_p(\infty) = 0, \quad \theta_p(\infty) = 0,
$$

Now calculating the residual errors and minimize over $\hbar_f, \hbar_g, \hbar_h$ & $\hbar_\theta$ in order to get the optimal values for $\hbar_f, \hbar_g, \hbar_h$ & $\hbar_\theta$ and the slightest possible error. In the process of error analyses, we have two methods namely, exact residual error and average residual error. For different order of approximation, CPU time required for evaluation of $f''(0), g'(0), \mathrm{h}'(0)$ and $\theta'(0)$ is observed. As for as CPU time is concerned, the average residual error needs less time compared to that of the exact residual error for increasing values of p. At p^{th} order deformation equation, the exact residual errors can be written as,

$$\bar{E}_p^f(\hbar_f) = \frac{1}{P+1}\sum_{y=0}^{P}\left(N_f\left[\hat{f}_{[P]}(\eta), \hat{g}_{[P]}(\eta), \hat{\theta}_{[P]}(\eta), \hat{\phi}_{[P]}(\eta)\right]\right)^2$$

$$\bar{E}_p^g(\hbar_g) = \frac{1}{P+1}\sum_{y=1}^{P}\left(N_g\left[\hat{g}_{[P]}(\eta), \hat{f}_{[P]}(\eta)\right]\right)^2$$

$$\bar{E}_p^\phi(\hbar_h) = \frac{1}{P+1}\sum_{y=0}^{P}\left(N_h\left[h_{[P]}(\eta), \hat{\theta}_{[P]}(\eta), \hat{f}_{[P]}(\eta)\right]\right)^2 \quad (25)$$

$$\bar{E}_p^\theta(\hbar_\theta) = \frac{1}{P+1}\sum_{y=0}^{P}\left(N_\theta\left[\hat{\theta}_{[P]}(\eta), \hat{f}_{[P]}(\eta), \hat{g}_{[P]}(\eta), h_{[P]}(\eta)\right]\right)^2$$

$$\bar{E}_p^t(\hbar) = \bar{E}_p^f(\hbar_f) + \bar{E}_p^g(\hbar_g) + \bar{E}_p^\theta(\hbar_\theta), \bar{E}_p^\phi(\hbar_\phi) \quad (26)$$

Here $\bar{E}_p^t(\hbar)$ gives the total average squared residual error of the problem and

Mathematical symbols $\bar{E}_p^f, \bar{E}_p^g, \bar{E}_p^h$ *and* $\bar{E}_p^\theta$ denote the individual average squared residual errors, It is undeniably demonstrated that $\bar{E}_p^f, \bar{E}_p^g, \bar{E}_p^h, \bar{E}_p^\theta$ *and* $\bar{E}_p^t$ gradually declines when the order of the approximation rises, demonstrating the viability of OHAM (see Table 1 and Table 2), which demonstrates that OHAM exist successfully. Computational software like Mathematica is utilized to minimize these mistakes for $n = 1, 2, 3, \ldots$. the optimal value of $\hbar_f, \hbar_g, \hbar_h$ and $\hbar_\theta$ for f, g, h and θ is given by $dE_n^f(\hbar_f)/dh = 0, dE_n^g(\hbar_g)/dh = 0, dE_n^h(\hbar_g)/dh = 0$ and $dE_n^\theta(\hbar_\theta)/dh = 0$ respectively. Evidently, $\lim_{n\to\infty} E_n^f(\hbar_f) = 0, \lim_{n\to\infty} E_n^g(\hbar_g) = 0, \lim_{n\to\infty} E_n^h(\hbar_h) = 0$ and $\lim_{n\to\infty} E_n^\theta(\hbar_\theta) = 0$ corresponds to a convergent series solution.

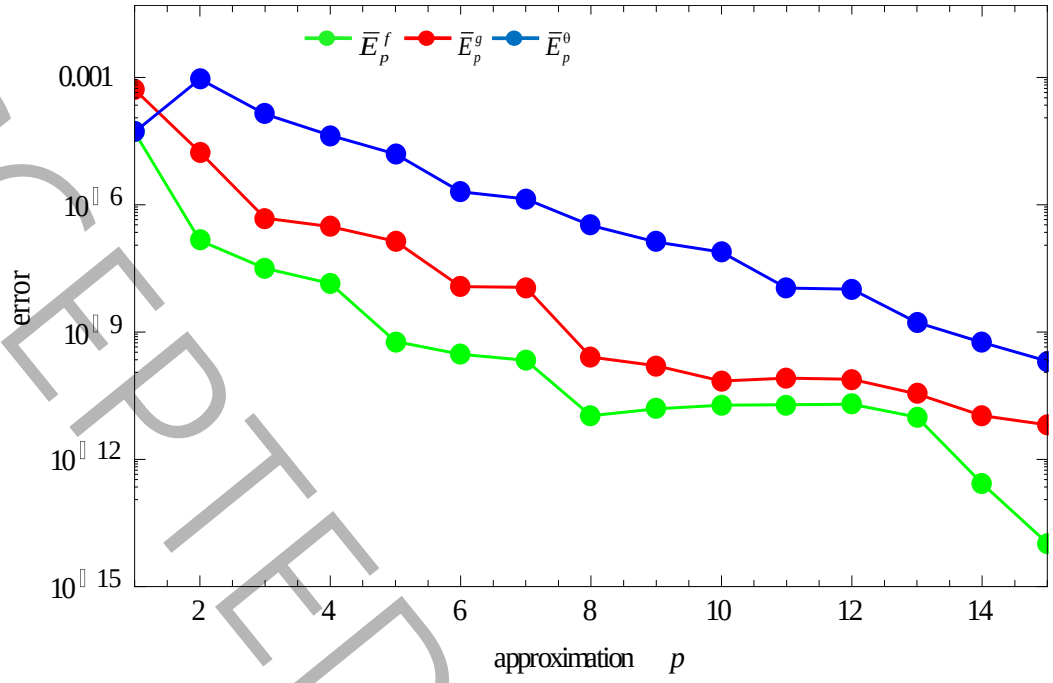

Fig. 1a. Individual residual error at a different approximation*p.*

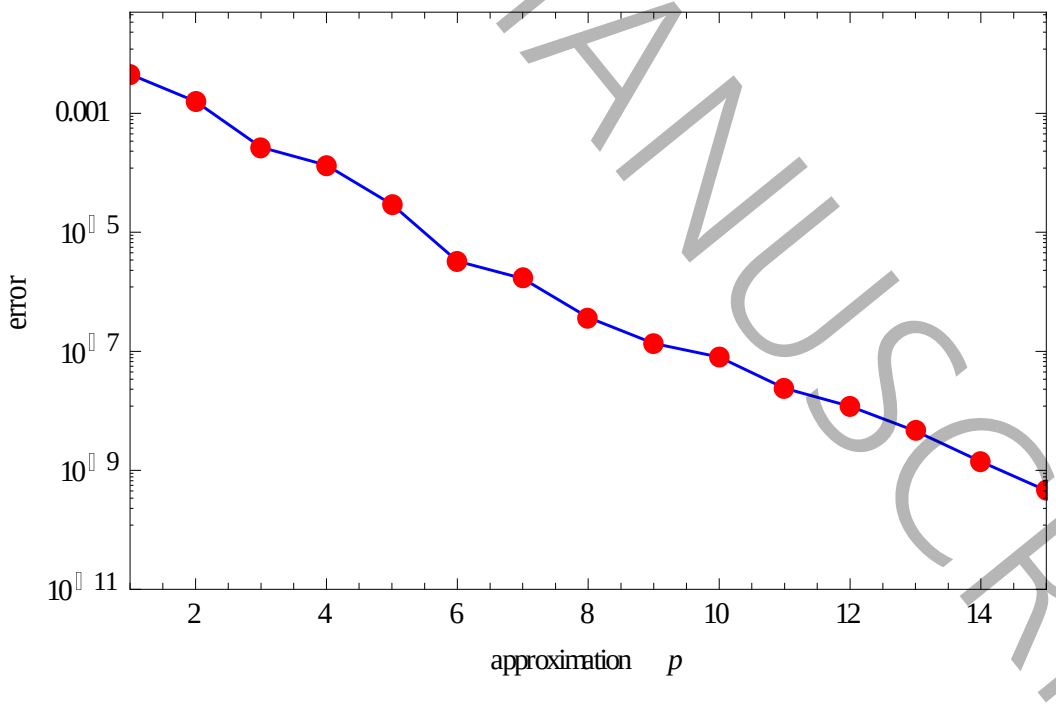

Fig.1b. Total residual error at a different approximation p

Table 1: Individual residual error at different approximation p.

p	$E_p^{\,f}(\hbar_f)$	$E_p^{\,\theta}(\hbar_g)$	$E_p^{\,\theta}(\hbar_\theta)$	CPU times **(S)**
1	5.165×10^{-5}	5.206×10^{-4}	5.192×10^{-4}	0.3692
3	3.183×10^{-8}	4.839×10^{-7}	1.377×10^{-4}	3.6593
5	5.992×10^{-10}	3.058×10^{-7}	1.156×10^{-4}	17.689
7	2.149×10^{-10}	1.138×10^{-8}	1.379×10^{-6}	69.350
9	1.554×10^{-11}	1.605×10^{-10}	1.320×10^{-7}	192.12
13	9.849×10^{-12}	3.475×10^{-11}	1.678×10^{-9}	1361.5
15	9.422×10^{-15}	5.322×10^{-12}	2.059×10^{-10}	4526.4

Table 2:Total residual error at a different approximation p

p	$-\hbar_f$	$-\hbar_g$	$-\hbar_\theta$	$E_p^{\,t}$	CPU times **(S)**
1	0.9008	0.4153	1.1176	1.377×10^{-3}	0.3692
3	0.9452	1.0053	1.1220	2.684×10^{-4}	3.6593
5	1.1395	1.0473	1.1192	1.672×10^{-6}	17.689
7	1.0609	1.0612	1.1582	1.356×10^{-7}	69.350
9	1.2150	1.0782	1.2062	2.391×10^{-8}	192.12
14	1.2255	1.1961	1.2749	1.403×10^{-9}	1361.5
15	1.2258	1.1596	1.2583	4.574×10^{-10}	4526.4

Confirming the Methodology:

Through both its convergence behavior and the comparison with reference solutions, the semi-analytical method's accuracy and stability of implementation are well established. In this work, a 15th-order OHAM approximation is carried out and the corresponding optimal convergence-control parameters are $\hbar_f = -1.2258$, $\hbar_g = -1.1596$, and $\hbar_\theta = -1.2583$. The residual error substantially decreases with increasing order of approximation, which indicates fast and stable convergence of the solution. This evolution is displayed in Figure 1(a-b) and the quantitative

results given in Table 1 and Table 2, respectively, where for each of the governing equations a uniform decrease of error is presented. The OHAM solutions obtained here are validated through systematic comparison with established numerical and analytical results from the open literature, and the close correspondence observed confirms the accuracy and reliability of the present approach. Tables 3 and 4 present quantitative comparisons showing that the computed values of skin friction and Nusselt number align closely with those reported by Kumar [17], Tripathy et al. [20], Chen [33], and Seddeek and Salem [34], with relative deviations remaining within acceptable numerical tolerance.

Table 3: Comparison of values of Skin-friction coefficient C_f^* with Kumar [17], Tripathy et al [20] and Fatunmbi and Okayo [24] (when n=0.5)

K	*M*	*Da*	Kumar [17]	Tripathy et al [20]	Fatunmbi and Okayo [24]	Present work
0	0	0	1.000000	1.000008	1.0000084	1.000000
0.5	0	0	0.880200	0.901878	0.8994515	0.899500
0.5	1.0	0	1.209900	1.250358	1.24966132	1.250100
0.5	1.0	1.0	----------	1.510062	1.5127320	1.512730
1.0	0.5	0	0.997600	0.995088	0.9919970	0.992650
1.0	0.5	1.0	----------	1.265126	1.2646592	1.265130

Table 4: Comparison of values of Nusselt number Nu_x^* with Chen [33], Seddeek and Salem [34] and Fatunmbi and Okayo [24].

Pr	Chen [33]	Seddeek and Salem [34]	Fatunmbi and Okayo [24]	Present work
0.72	1.08853	1.08852	1.088525691	1.09258
1.0	1.33334	1.33333	1.33333333	1.33332
3	2.50972	2.50972	2.50972521	2.50969
7	3.97150	3.97150	3.917151157	4.00023
10	4.79686	4.97151	4.79687327	4.79686

4. Flow Analysis and Discussions

To explore the model predictions, a range of physical parameter values have been calculated following the method described in section 3. The relationships between the speed and micro-rotational speed vs. viscosity h are presented in the plots in Figure 2-4. The graph (Figure 2) clearly shows that for higher values of viscosity h (i.e., $h = 0,1,2$), the thickness of boundary layer of the velocity profile $f'(\eta)$ decreases. This is due to the higher h shows low temperature difference between the liquid and the plate, which leads to the increase of viscosity h of the liquid and consequently enhances both thermal profiles $\theta(\eta)$ and micro velocity profile $g(\eta)$ (see Figure 3&Figure 4).According to Figures. 5-7, we found that when we increase the value to a higher value of K then the thermal $\theta(\eta)$ boundary layer thickness and velocity $f'(\eta)$ boundary surfaces can be increased except for the micro velocity profile $g(\eta)$. The micropolar parameter K represents the relative contribution of micro-rotation (microstructure effects) compared to classical viscous effects. When K (K>0) increases, the effective resistance of the fluid to shear decreases because part of the momentum is transferred into particle rotation, which weakens the classical viscous stress. As a result, the horizontal velocity increases and the momentum boundary layer becomes thicker compared with the Newtonian case (K=0) far from the wall, where shear-induced microrotation diminishes, the fluid gradually recovers viscous-dominated behavior analogous to a Newtonian medium. Figure 8 illustrates the response of the velocity field to variations in the Darcy permeability number Da; higher Da values correspond to a more permeable porous medium, which reduces flow resistance and consequently augments the axial velocity throughout the boundary layer. Figure 9 demonstrates that strengthening the applied magnetic field (larger M) progressively suppresses the fluid velocity, a consequence of the retarding Lorentz force generated by the interaction of the magnetic field with the electrically conducting fluid. The influence of the micropolar boundary parameter n on the micro-rotational velocity profile is illustrated in Figure 10. Physically, the parameter n represents the micropolar boundary parameter and varies within the range $0 \le n \le 1$. At n = 0 the microelements at the solid surface are constrained from rotating, corresponding to a physical scenario of dense particle packing at the wall where rotational freedom is suppressed. The case n = 0.5 is often associated with turbulence-like behavior in the boundary layer, where micro-rotation effects are more pronounced. When n=1, it characterizes a weak concentration of microelements at the wall, corresponding to a stress-free or free-spin condition, and it controls the micro-rotation boundary behavior in the governing equations. The velocity profile clearly increases as a function of the boundary parameter

value. Figure 11 shows an increase in the temperature profile when $\varepsilon(i.e., \varepsilon = 0, 1, 2)$ is changed in thermal conductivity. With comes also temperature graph/thermal boundary surface due to linear heat& especially fluids with poor thermal conductivity, which cool faster. It is clear from Figure 12, as Nr increases, the optically thick medium becomes progressively more transparent to radiation; the effective Rosseland mean absorption decreases, amplifying the divergence of the radiative heat flux and transferring additional thermal energy into the fluid, thereby thickening the thermal boundary layer. Furthermore, increase in Nr contributes to the conduction effect, which leads to an increase in temperature everywhere away from the sheet. Additionally, the Nr modifies behavior underscores the strong coupling between the radiation parameter and the thermal field; even modest increases in Nr substantially reshape the temperature profile and expand the thermal boundary layer, confirming the dominant role of radiation in thermally thick flow regimes. Figure 13 indicates that an increase Pr leads to a softening of the temperature profile and to a thinner thermal boundary layer. physically, a higher Prandtl number Pr implies reduced thermal diffusivity relative to momentum diffusivity, which confines the thermal disturbance to a narrower region near the wall, resulting in steeper temperature gradients and faster surface cooling. Figs. 14 and 15 demonstrate opposite thermal responses to the Eckert number Ec $(\mathrm{i.e.}, \mathrm{Ec} = 0,1,1.5)$ and heat source/sink parameter Q. An increasing Ec enhances viscous dissipation, elevating the fluid temperature in regions of intense shearing. Conversely, positive Q acts as an internal heat source (fluid heating), while negative Q reflects an energy sink (fluid cooling), yielding contrasting thermal boundary layer responses. Moreover, the relative influence of viscous dissipation and thermal radiation on the thermal field. The discussion now highlights that viscous dissipation contributes to internal heat generation through the Eckert number, thereby enhancing the fluid temperature particularly in regions of strong velocity gradients near the surface, while thermal radiation influences the temperature distribution by modifying the effective thermal energy transport within the boundary layer. An overview of the effect of various physical parameters on the variation of local skin friction and temperature gradient at the surface is presented in Table 5.

Concluding remarks

The current study examines how a thermally radiating magneto micropolar fluid behaves when it passes through a linearly stretched sheet that is embedded in a porous material. OHAM can be used to get semi-analytical solutions of the governing highly nonlinear differential equations. The effect of the controlling parameters has been examined and discussed through graphs & tables. The main findings in this study are mentioned below:

- The micropolar fluid model produces a thicker velocity boundary layer relative to its Newtonian counterpart under identical flow conditions, attributable to the additional momentum imparted by microrotational effects.
- The thermal transport efficiency progressively diminishes with increasing values of the micropolar parameter K, as the enhanced rotational inertia redirects energy from thermal conduction into particle rotation.
- The skin friction coefficient and Nusselt number exhibits opposite trend for enhancing values of h and ε.
- The thermal boundary layer expands monotonically with increasing Eckert number and radiation parameter, reflecting enhanced internal energy generation and radiative heating; however, elevation of the Prandtl number suppresses thermal diffusion, producing a contraction of the thermal layer.

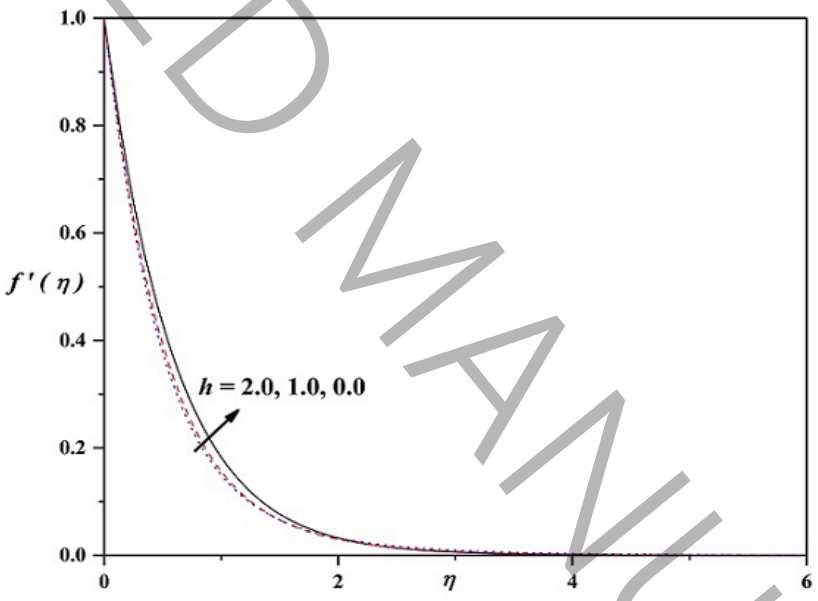

Fig.2: Impact of viscosity parameter *h* on the field of velocity $f'(\eta)$ with

$$K = M = n = \varepsilon = Nr = Ec = Q = 0.5, Da = 2, \Pr = 0.72$$

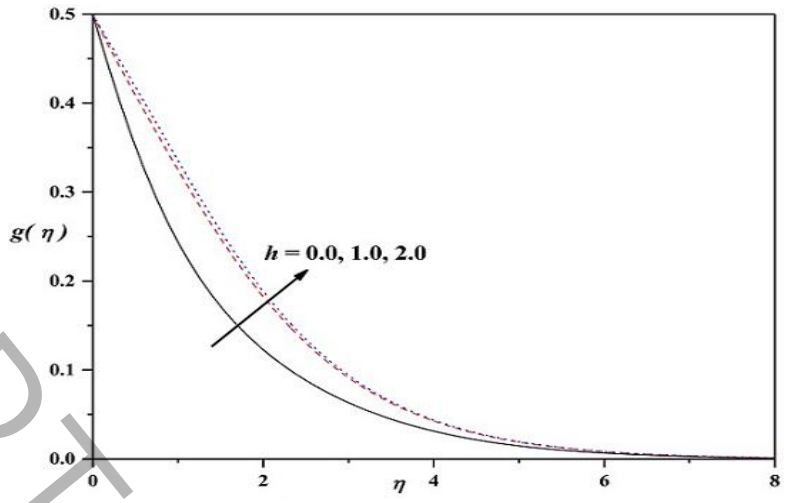

Fig.3: Effect of viscosity parameter *h* on the field of velocity $g(\eta)$ with

$K = M = n = \varepsilon = Nr = Ec = Q = 0.5, Da = 2, \Pr = 0.72$

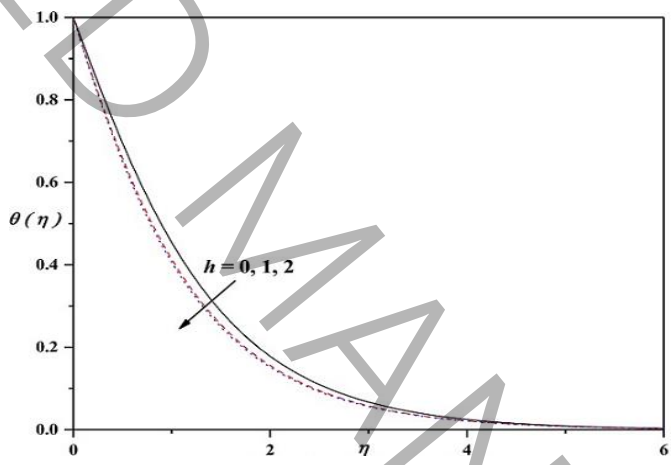

Fig.4: Variation of viscosity parameter *h* on the field of temperature $\theta(\eta)$ with

$K = M = n = \varepsilon = Nr = Ec = Q = 0.5, Da = 2, \Pr = 0.72$

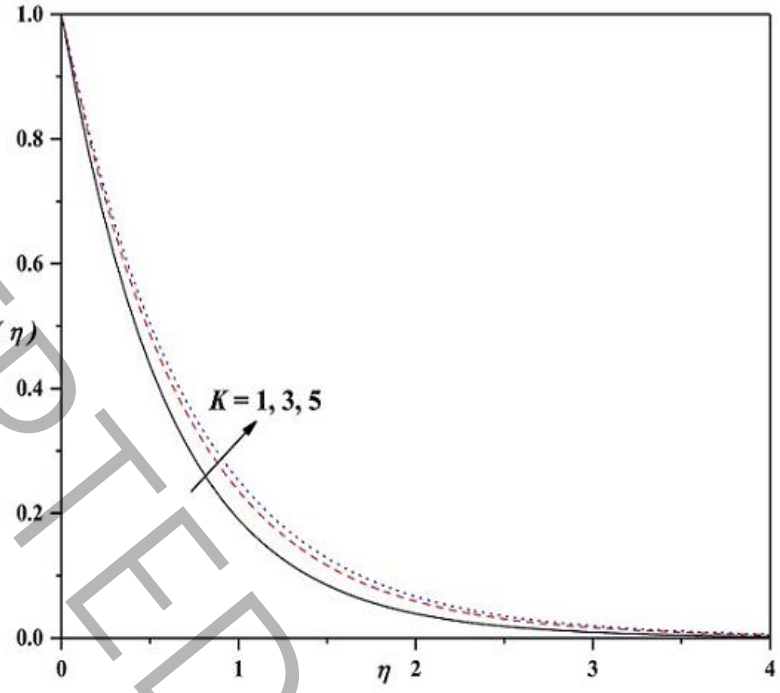

Fig.5: Impact of micropolar parameter K on the field of velocity $f'(\eta)$ with

$$h = M = n = \varepsilon = Nr = Ec = Q = 0.5, Da = 2, \Pr = 0.72$$

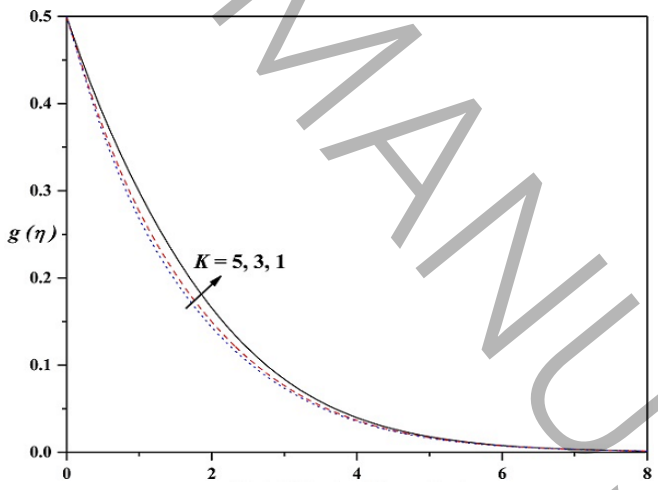

Fig.6: Effect of micropolar parameter K on the field of velocity $g(\eta)$ with

$$h = M = n = \varepsilon = Nr = Ec = Q = 0.5, Da = 2, \Pr = 0.72$$

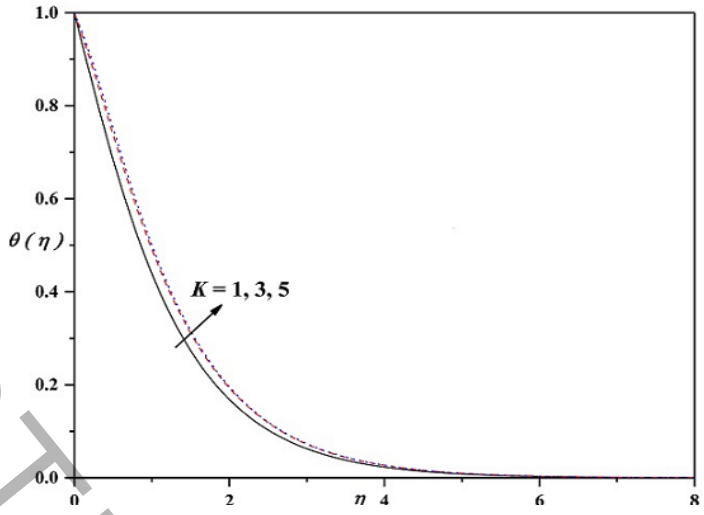

Fig.7: Impact of micropolar parameter K on the field of thermal $\theta(\eta)$ with

$$h = M = n = \varepsilon = Nr = Ec = Q = 0.5, Da = 2, \Pr = 0.72$$

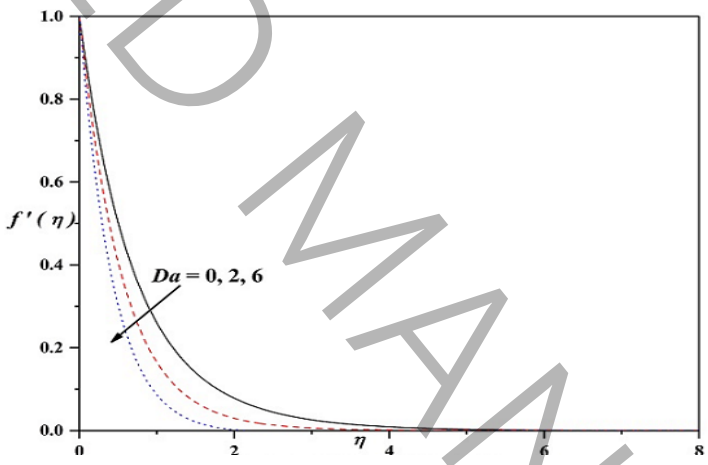

Fig.8: Variation of Darcy parameter Da on the field of velocity $f'(\eta)$ with

$$K = h = M = n = \varepsilon = Nr = Ec = Q = 0.5, \Pr = 0.72$$

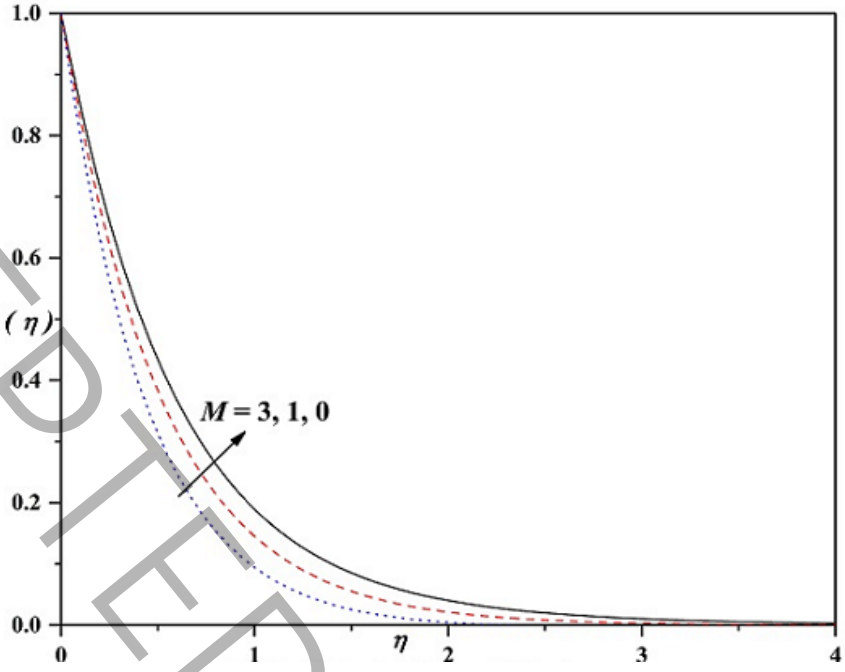

Fig.9: Impact of magnetic parameter M on the field of velocity $f'(\eta)$ with

$$K = h = n = \varepsilon = Nr = Ec = Q = 0.5, Da = 2, \Pr = 0.72$$

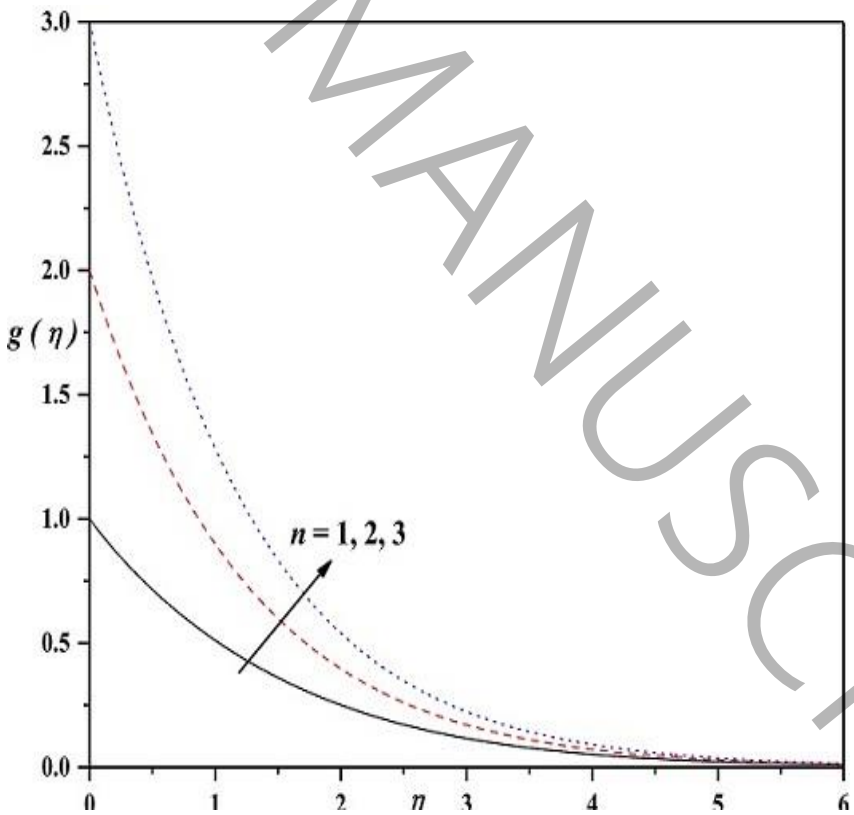

Fig.10: Effect of micropolar boundary parameter n on the field of velocity $g(\eta)$ with

$K = h = M = \varepsilon = Nr = Ec = Q = 0.5, Da = 2, \Pr = 0.72$

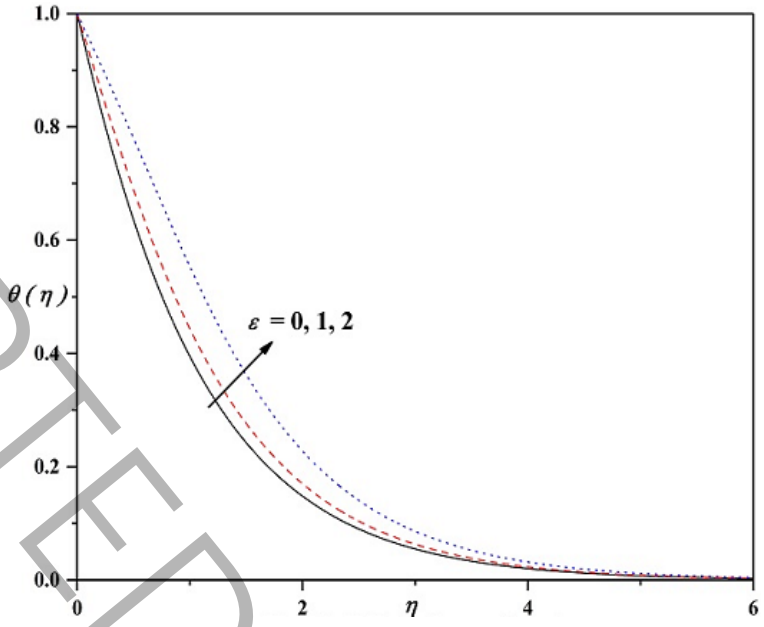

Fig.11: Impact of thermal dependent viscosity parameter ε on the field of temperature $\theta(\eta)$ with $K = h = M = n = Nr = Ec = Q = 0.5, Da = 2, \Pr = 0.72$

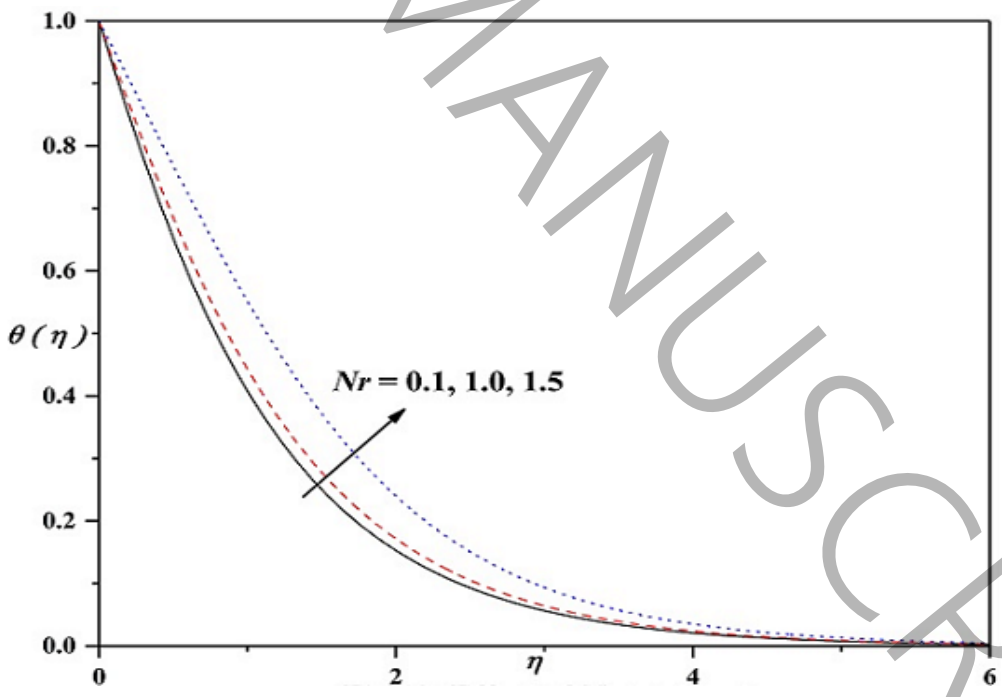

Fig.12: Variation of radiation parameter Nr on the field of temperature $\theta(\eta)$ with $K = h = M = n = \varepsilon = Ec = Q = 0.5, Da = 2, \Pr = 0.72$

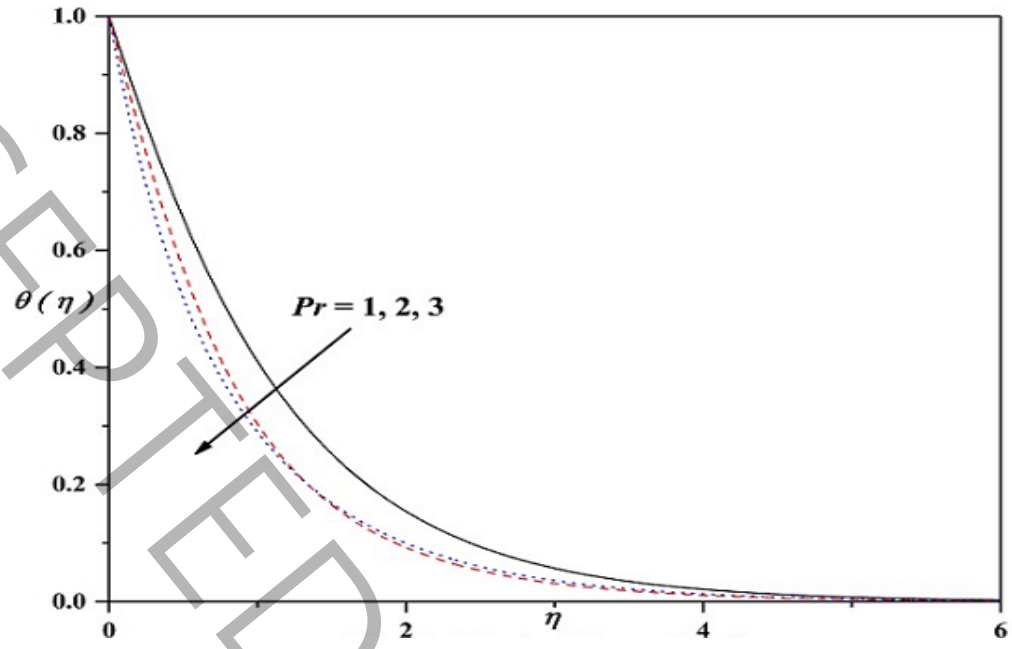

Fig.13: Impact of thermal dependent viscosity parameter Pr **on the field of temperature** $\theta(\eta)$ **with** $K = h = M = n = \varepsilon = Nr = Ec = Q = 0.5, Da = 2$

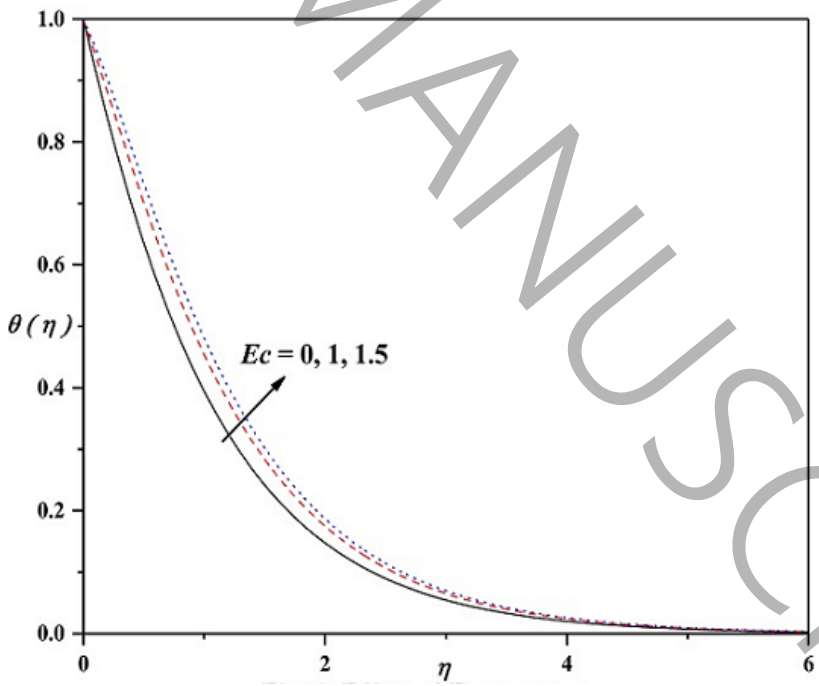

Fig.14: Impact of Eckert number Ec **on the field of temperature** $\theta(\eta)$ **with**

$K = h = M = n = \varepsilon = Q = 0.5, Da = 2, \Pr = 0.72$

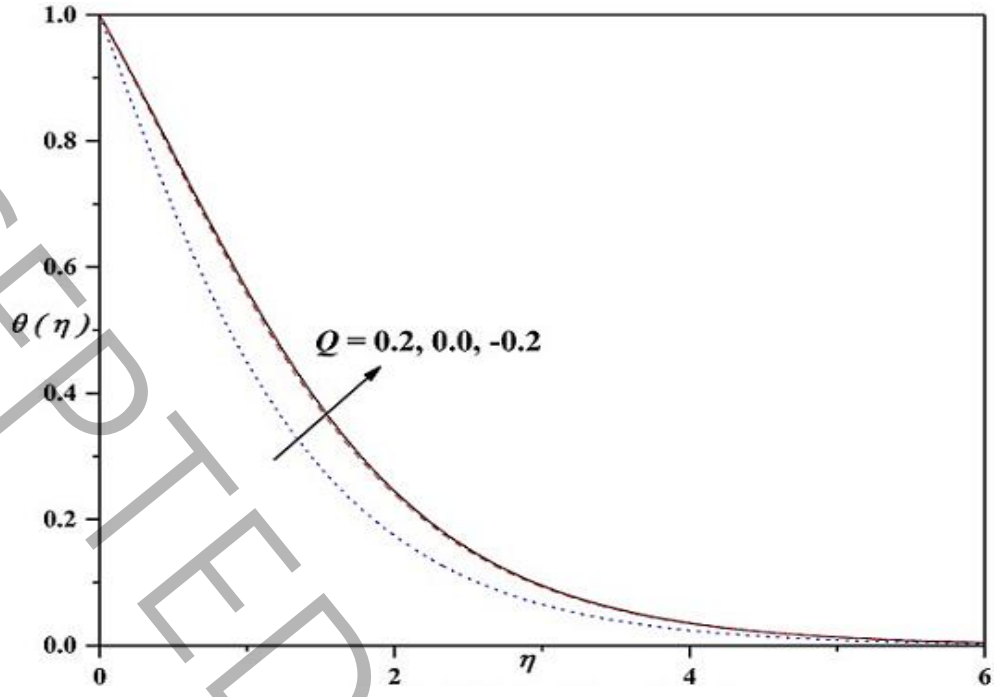

Fig.15: Impact internal heat source/sink parameter Q on the field of temperature $\theta(\eta)$ with $K = h = M = n = \varepsilon = Ec = 0.5, Da = 2, \Pr = 0.72$

Declarations:

Conflicts of Interest
The authors declare that there are no conflicts of interest.

Acknowledgements
The authors declare that no funding was received for conducting the research or preparing this article.

ORCID ID: https://orcid.org/0000-0003-4470-2074- Dr. Hussain Basha

Author Contributions:

Dr. Hussain Basha has contributed to the conceptualization, mathematical modeling, and analytical solution using OHAM. **Dr. V. Ramanjini** has handled result analysis, graphical interpretation, and manuscript refinement.

References

[1]. B.C. Sakiadis, Boundary-layer behavior on continuous solid surfaces, AIChE Journal, 7 (1961) 26–28.

[2]. L.J. Crane, Flow past a stretching plate, Zeitschrift für Angewandte Mathematik und Physik, 21 (1970) 645–647.

[3]. P.S. Gupta, A.S. Gupta, Heat and mass transfer on a stretching sheet with suction or blowing, Canadian Journal of Chemical Engineering, 55 (1977) 744–746.

[4]. L.J. Grubka, K.M. Bobba, Heat transfer characteristics of a continuous stretching surface with variable temperature, ASME Journal of Heat Transfer, 107 (1985) 248–250.

[5]. B.K. Dutta, P. Roy, A.S. Gupta, Temperature field in the flow over a stretching sheet with uniform heat flux, International Communications in Heat and Mass Transfer, 12 (1985) 89–94.

[6]. C.K. Chen, M.I. Char, Heat transfer of a continuous stretching surface with suction or blowing, Journal of Mathematical Analysis and Applications, 135 (1988) 568–580.

[7]. M.E. Ali, Heat transfer characteristics of a continuous stretching surface, Heat and Mass Transfer, 29 (1994) 227–234.

[8]. C.H. Chen, Laminar mixed convection adjacent to vertical continuously stretching sheet, Heat and Mass Transfer, 33 (1998) 471–476.

[9]. H. Vaidya, K.V. Prasad, K. Vajravelu, S.A. Shehzad, H. Basha, Role of variable liquid properties in 3D flow of Maxwell nanofluid over convectively heated surface: Optimal solutions, Journal of Nanofluids, 8 (2019) 1133–1146.

[10]. K.V. Prasad, H. Vaidya, K. Vajravelu, G. Manjunatha, M. Rahimi-Gorji, H. Basha, Heat transfer analysis of three-dimensional mixed convective flow of an Oldroyd-B nanoliquid over a slippery stretching surface, Defect and Diffusion Forum, 401 (2020) 164–182.

[11]. K.V. Prasad, H. Vaidya, O.D. Makinde, K. Vajravelu, A. Wakif, H. Basha, Comprehensive examination of the three-dimensional rotating flow of a UCM nanoliquid over an exponentially stretchable convective surface utilizing the Optimal Homotopy Analysis method, Frontiers in Heat and Mass Transfer, 14 (2020) 1–12.

[12]. H. Basha, Significance of variability in liquid properties on 3D MHD Maxwell nanofluid flows over a stretching surface with heat generation/absorption and chemical reaction, Journal of Nanofluids, 13 (2024) 15–27.

[13]. H. Basha, Heat and mass transport phenomenon on 3D MHD Jeffery nano-liquid past an exponentially stretchable sheet subject to Soret and Dufour effect: optimal solutions, Zeitschrift für Angewandte Mathematik und Mechanik, 104 (2024) e2300602.

[14]. A.C. Eringen, Simple microfluids, International Journal of Engineering Science, 2(2) (1964) 205–217.

[15]. A.C. Eringen, Theory of micropolar fluids, Journal of Applied Mathematics and Mechanics, 16(1) (1966) 1–18.

[16]. R.S.R. Gorla, R. Pender, J. Eppich, Heat transfer in micropolar boundary layer flow over a flat plate, International Journal of Engineering Science, 21(7) (1983) 791–798.

[17]. L. Kumar, Finite element analysis of combined heat and mass transfer in hydromagnetic micropolar flow along a stretching sheet, Computational Materials Science, 46(4) (2009) 841–848.

[18]. M. Ashraf, A.R. Wehgal, MHD flow and heat transfer of micropolar fluids between two porous disks, Applied Mathematics and Mechanics (English Edition), 33(1) (2012) 51–64.

[19]. M. Qasim, I. Khan, S. Shafie, Heat transfer in a micropolar fluid over a stretching sheet with Newtonian heating, PLOS ONE, 8(3) (2013) 59393.

[20]. R.S. Tripathy, G.C. Dash, S.R. Mishra, M.M. Hoque, Numerical analysis of hydromagnetic micropolar fluid along a stretching sheet embedded in porous medium with nonuniform heat source and chemical reaction, Engineering Science and Technology, an International Journal, 19(3) (2016) 1573–1581.

[21]. S.R. Mishra, I. Khan, Q.M. Al-mdallal, T. Asifa, Free convective micropolar fluid flow and heat transfer over a shrinking sheet with heat sources, Case Studies in Thermal Engineering, 11 (2018) 113–119.

[22]. H. Rosali, A. Ishak, I. Pop, Micropolar fluid flow towards a stretching sheet in a porous medium with suction, International Communications in Heat and Mass Transfer, 39 (2012) 826–829.

[23]. E.O. Fatunmbi, A. Adeniyan, Nonlinear thermal radiation and entropy generation on steady flow of magneto micropolar fluid passing a stretchable sheet with variable fluid properties, Results in Engineering, 6 (2020) 100142.

[24]. E.O. Fatunmbi, S.S. Okoyo, Heat transfer in boundary layer magneto micropolar fluids with temperature-dependent properties over a stretching sheet, Advances in Materials Science and Engineering, 1 (2020) 1–11.

[25]. S. Khattak, M.N. Khan, M.B. Riaz, D. Lu, M. Hussien, M.D. Albalwi, A. Jhangeer, Insights of temperature-dependent fluid characteristics on micropolar material in a rotating frame with cubic autocatalysis chemical reaction, Journal of Computational Design and Engineering, 11(5) (2024) 29–39.

[26]. S. Alao, S.O. Salawu, R.A. Oderinu, A.A. Oyewumi, E.I. Akinola, Investigation of thermal radiation and viscous heating effects on the hydromagnetic reacting micropolar fluid species flowing past a stretchy plate in permeable media, International Journal of Thermofluids, 22 (2024) 100600.

[27]. S. Liao, An optimal Homotopy-analysis approach for strongly nonlinear equations, Communications in Nonlinear Science and Numerical Simulation, 15 (2010) 2003–2016.

[28]. T. Fan, X. You, Optimal homotopy analysis method for nonlinear differential equations in the boundary layer, Numerical Algorithms, 62(2) (2013) 337–354.

[29]. K.V. Prasad, H. Vaidya, K. Vajravelu, V. Ramanjini, Analytical study of Cattaneo-Christov heat flux model for Williamson-nanofluid flow over a slender elastic sheet with variable thickness, Journal of Nanofluids, 7 (2018) 583–594.

[30]. R.A. Van Gorder, Optimal homotopy analysis and control of error for implicitly defined fully nonlinear differential equations, Numerical Algorithms, 81 (2019) 181–196.

[31]. H. Basha, V. Ramanjini, M.K. Sahukar, Enhancement of heat and mass transfer in 2D-mixed convection nano-liquid flow over a flexible Riga plate with heat source/sink and chemical reaction, Journal of Nanofluids, 13(3) (2024) 749–759.

[32]. H. Basha, Influence of variable fluid properties on MHD three dimensional (3D) Maxwell nano-liquid flow over convectively heated stretchable Riga plate with thermal radiation and Soret-Dufour phenomena, Journal of Nanofluids, 14 (2025) 81–94.

[33]. C.H. Chen, Laminar mixed convection adjacent to vertical, continuously stretching sheets, Heat and Mass Transfer, 33(5-6) (1998) 471–476.

[34]. M.A. Seddeek, A.M. Salem, Laminar mixed convection adjacent to vertical continuously stretching sheets with variable viscosity and variable thermal diffusivity, Heat and Mass Transfer, 41(12) (2005) 1048–1055.

Table5: Computed values of skin-friction coefficient, Nusselt number and wall couple stress (C_f^*, Nu_x^* and C_s^*) for different values pertinent parameters.

h	K	M	Da	ε	Nr	Pr	Ec	Q	n	C_f^*	Nu_x^*	C_s^*
0	0.5	0.5	2	0.5	0.5	0.72	0.5	0.5	0.5	-1.6790	-0.3308	-0.6411
2										-1.9556	-0.1742	-0.7875
2.5										-1.9828	-0.1695	-0.7935
0.5	1									-1.6454	-0.2533	-0.6600
	3									-1.4238	-0.2753	-0.4480
	5									-1.3524	-0.2839	-0.3672
	0.5	0								-1.6708	-0.2551	-0.7491
		1								-1.9149	-0.2412	-0.7053
		3								-2.3180	-0.2182	-0.6104
		0.5	0							-1.4036	-0.2719	-0.7829
			2							-1.7975	-0.2479	-0.7283
			6							-2.3651	-0.2999	-0.5922
			2	0						-1.8019	-0.2473	-0.8692
				1						-1.7961	-0.2484	-0.6451
				2						-1.7861	-0.2488	-0.4216
				0.5	0.1					-1.7994	-0.2475	-0.7796
					1					-1.7972	-0.2483	-0.6721
					1.5					-1.7947	-0.2485	-0.4656
					0.5	0.72				-1.6790	-0.3308	-0.3308
						1				-1.8024	-0.2471	-0.7775
						2				-1.8240	-0.2421	-1.0030
						0.72	0			-1.8034	-0.2473	-0.8742
							1			-1.7914	-0.2485	-0.5697
							1.5			-1.7852	-0.2490	-0.4154
							0.5	-0.2		-1.7952	-0.2483	-0.4161
								0		-1.7958	-0.2482	-0.4328
								0.2		-1.7965	-0.2481	-0.6391
								0.5	1	-1.7952	-0.2483	-0.4161
									2	-1.7958	-0.2482	-0.4328
									3	-1.7965	-0.2481	-0.6391

Nomenclature

$a, A \& D$	Constants
$B \& B_0$	Magnetic field and Magnetic Field strength
C_p	Specific heat at constant temperature
Da	Darcy parameter
Ec	Eckert number
f	Dimensionless horizontal velocity
g	Dimensionless micro rotational velocity
h	Temperature dependent viscosity parameter
j	Micro inertial density
k	Vertex velocity
K	Micro polar parameter
K_p	Permeability of the porous medium
$K(T)$	Thermal conductivity
K_∞	Thermal conductivity for away from the wall
l	Characteristic length
M	Magnetic parameter
n	Micro polar boundary parameter
N	Micro rotation parameter
Nr	Radiation parameter
Pr	Prandtl number
Q	Heat source/sink parameter
q_w	Heat flux
T	Fluid temperature
T_w	Temperature at wall
T_∞	Free stream temperature
U_w	Free Stream velocity
u & v	Velocity components along x & y directions respectively

Greek symbols

α	Micro absorption coefficient
γ	Spin gradient velocity
$\mu(T)$	Viscosity of the fluid
μ_0	Ambient fluid
η	Similarity variable
ρ	Density of the fluid
θ	Dimensionless Temperature
σ	Stefan Boltzmann constant
τ	Ratio between the effective heat capacity of the nanoparticle substance and heat capacity of the base fluid